scientific reports

OPEN

Effect of aluminum and ammonium perchlorate particle sizes on the condensed combustion products characteristics of aluminized NEPE propellants

Chengyin Tu[1], Xiong Chen[1]✉, Fan Chen[2], Yuqian Zhuang[1], Wenxiang Cai[1], Yingkun Li[1], Weixuan Li[1], Changsheng Zhou[1] & Renjie Xie[1]

Aluminum (Al) is usually added to solid propellants to improve the combustion performance, however the condensed combustion products (CCPs) especially the large agglomerates generated from aluminum combustion can reduce the specific impulse of the engine, and result in two-phase loss, residue accumulation and throat liner ablation. Al and ammonium perchlorate (AP), as important components of NEPE propellants, can affect the formation process of the CCPs of aluminized NEPE propellants. To clarify the effect of Al and AP particle sizes on the properties of the CCPs of aluminized NEPE propellants, a constant-pressure quench vessel was adopted to collect the combustion products of four different formulations of NEPE propellants. It was found that the condensed combustion products are mainly divided into aluminum agglomerates and oxide particles, the diameter of the aluminum agglomerates of these four different formulations of NEPE propellants at 7 MPa was smaller than that in 3 MPa, and the shells of the aluminum agglomerates were smoother and the spherical shape was more perfect. X-ray diffraction analysis of the CCPs of the four NEPE propellants under 3 MPa revealed the presence of both Al and Al_2O_3. With the increase of the particle size of Al and AP, the oxidation degree of aluminum particles decreases. The particle size of the CCPs of the four different formulations of NEPE propellants under 1 and 3 MPa was analyzed by using a laser particle size analyzer, it is found that the increase of AP particle size is helpful to reduce the size of condensate combustion products. Based on the classical pocket theory, establishing a new agglomeration size prediction model, which can be used to predict the agglomeration size on the burning surface. Compared with the empirical model, the new agglomeration size prediction model is in good agreement with the experimental results.

Keywords Al particle, AP particle, NEPE propellant, Condensed combustion products, Al agglomeration

Aluminum (Al) powder is usually added to solid propellants to improve the energy density of the solid propellant and the specific impulse of the motor. However, the Al particles may form large sized aluminum agglomerates during the propellant combustion process. Large aluminum aggregates of the condensed combustion products (CCPs) will cause many adverse effects on the combustion process of the motor system. For instance, CCPs have a strong impact on the inner wall of the motor, which can aggravate the ablation of the insulation layer and throat liner, cause slag deposition, and affect the safety of the motor[1–3]. It has been reported that for every 10% of unburned aluminum, there is 1% loss in specific impulse (I_{sp})[4]. Therefore, gaining deep insight in the physical and chemical properties of CCPs is helpful to provide theoretical support for the performance improvement of solid rocket motor.

The agglomeration process of aluminum particles typically occurs on the burning surface of propellants and can be divided into three stages: accumulation, aggregation, and agglomeration. Currently, research on aluminum

[1]School of Mechanical Engineering, Nanjing University of Science and Technology, Nanjing 210094, People's Republic of China. [2]Wuhan Guide Infrared Co.,Ltd., Wuhan 430205, People's Republic of China. ✉email: chenxiongnjust@njust.edu.cn

particle agglomeration mainly falls into two ways: online testing and offline analysis. Online testing methods can capture the agglomeration process of Al particles on the propellant burning surface. This allows for the observation of the morphological evolution, combustion characteristics, and size distribution of agglomerates without disturbing the combustion of the solid propellant itself[5,6]. However, most experimental studies on the agglomeration process have been conducted under relatively low-pressure conditions. There is a lack of research that simulates the high-temperature (2700–3000 K) and high-pressure (40–100 atm) working environment of solid rocket motors.

Compared with online testing methods, offline analysis of CCPs can provide a more comprehensive understanding of the agglomerates properties, such as particle size distribution, composition, and microstructure. Researchers primarily study the agglomeration characteristics of Al particles in CCPs using the quench-collection method. Sambamurthi et al.[7] investigated the agglomeration process of aluminum particles in propellants through a plume quench-particle collection setup, the results showed that changes in pressure and oxidizer particle size can affect the size of CCPs. Babuk et al.[8] used a constant-volume quenching technique to collect CCPs. Glotov et al.[9] analyzed the influence of factors such as the distance from the burning surface to the coolant, type of oxidizer, and type of coolant on the agglomerates using quenching techniques. Anand et al.[10]collected the CCPs of sixteen kinds of solid propellants at pressures ranging from 2 to 10 MPa. They conducted comparative studies on the effects of factors such as coarse AP particle size, fine AP content, aluminum particle size, and propellant burning rate on the size distribution of agglomerates. Many studies have shown that the factors affecting the particle size distribution of solid propellant combustion products include the size of the aluminum particles and their percentage[7,10–15], the size of AP particles[8,10,11], fraction of coarse and fine AP particles[7,10,14,16], oxidizer types[8,13,17], binder properties[13], distance from the burning surface[18], burning atmosphere[19], chamber pressure[7,8,11,12,18,20], and burning rate of the propellant[10,15].

The ignition, combustion, and agglomeration processes of aluminum particles on the propellant burning surface are highly complex[21]. Currently, there is no comprehensive and detailed mathematical model that can describe the size of aluminum agglomerates. A number of scholars have conducted extensive research on aluminum agglomeration models, which can be divided into four categories: empirical models[22–25], pocket models[12,26–28], physical models[8,29,30], and random packing models[31–34]. Empirical models are mainly represented by Willoughby[22], Salita[23], Beckstead[24], and others. Cohen[25] modified Beckstead's agglomeration model by incorporating the effects of pressure and aluminum particle size on the particle size distribution of CCPs based on empirical models. However, empirical models don't consider the physical process of aluminum particle agglomeration and can't calculate the particle size distribution of agglomerates. In 1966, Crump[26] first proposed the conception of the pocket model, which addressed the shortcomings of empirical models. It is one of the most classic and widely accepted agglomeration models. In 1982, Cohen[12] and Grigoriev[27] conducted more in-depth quantitative research based on Crump's work and improved the pocket model to make it more universal. In 1999, Babuk[8] introduced the concept of a physical model, which considers the complex physicochemical processes of aluminum agglomeration. However, the physical model does not take into account the adhesive forces between aluminum agglomerates and the burning surface or the lift forces exerted by the gas flow on the agglomerates. In 2005, Jackson et al.[31] proposed the random packing model, which can be used to predict the particle size distribution of aluminum agglomerates. However, it heavily relies on the selection of certain parameters, which can lead to significant deviations in the predicted results. Indeed, the four widely used aluminum agglomeration models each have their own characteristics and limitations. Future research in this area should focus on establishing a mathematical model that can accurately predict the particle size distribution of aluminum agglomerates while maintaining high computational efficiency.

Based on this, this paper aims to gain a deeper understanding of the agglomeration behavior and mechanism of aluminum particles. By collecting the CCPs of aluminized NEPE propellant after combustion, the microstructure of the CCPs is observed by using a scanning electron microscope (SEM) and an accompanying X-ray energy dispersive spectrometer. The crystal phase composition of the CCPs is analyzed by using an X-ray diffractometer. The particle size of aluminum agglomerates is measured by using a laser particle size analyzer to study the agglomeration characteristics of aluminum particles. Simultaneously, proposing a mathematical model for aluminum particle agglomeration, through experimental measurements of aluminum agglomerate size distribution, combined with theoretical analysis and experimental results, verifying the mathematical model that can better predict the size of agglomerates and provide a theoretical basis for improving the performance of aluminized NEPE propellants.

Experimental

Samples

Figure 1 shows four kinds of NEPE propellants used in this study, numbered from JF-1 to JF-4. The difference of grain size distribution causes their different colors. The basic components of four kinds of NEPE propellants include oxidizing agent (ammonium perchlorate, AP, 15%), energetic plasticizers (nitroglycerin/butanetriol trinitrate, NG/BTTN, 15%), cross-linking agents (glycidyl azide polyether, GAP, 7%), metal fuel (Al, 20%), high-energy explosive (cyclotetramethyle tetranitramine and hexanitrohexaazaisowurtzitane, HMX&CL-20, 40%), and a small proportion of other additives. Table 1 gives information of grain sizes of four kinds of tested NEPE propellants. Samples adopted in this experiment were typically 5 mm × 5 mm × 10 mm rectangular bars.

The propellant is prepared according to the following procedures: First, mixed solid materials are added to the prepared liquid material, and then all materials are mixed in a vertical kneader for 1 h. Second, the obtained propellant slurry is degassed and cured in a vacuum oven at 50 ℃ for 7 days. Finally, the propellant is cut into samples of the required size to meet the needs of the experiment.

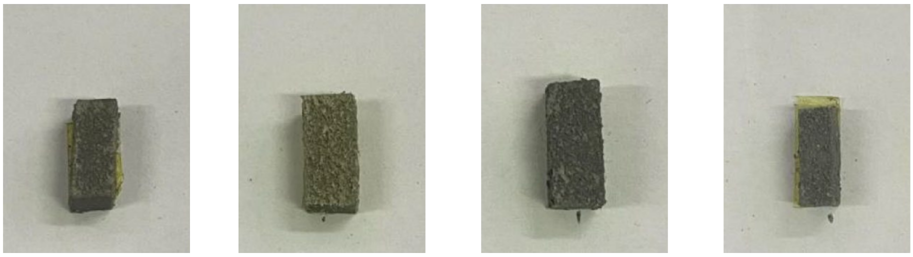
(a)JF-1 (b)JF-2 (c)JF-3 (d)JF-4

Figure 1. Pictures of NEPE propellant specimen.

Sample	Al	Ammonium nitrate explosive	AP
JF-1	3 μm	HMX&CL-20(50 μm)	200–300 μm
JF-2	30 μm	HMX&CL-20(50 μm)	200 –300 μm
JF-3	3 μm	HMX&CL-20(50 μm)	300 –400 μm
JF-4	3 μm	HMX&CL-20(50 μm)	400 –500 μm

Table 1. Grain sizes of four kinds of tested NEPE propellants.

Experimental apparatus

The schematic diagram of the experimental apparatus is shown in Fig. 2. It consists of a CO_2 laser, a combustion chamber, and a combustion product collection system. The control system, composed of computer software and control cards, can be used to adjust the laser loading time and heat flux density of the CO_2 laser. The power of the CO_2 laser used in the experiment is 300 W, with a wavelength of 10.6 μm and a laser beam diameter of Φ4 mm. The optical system consists of a flat mirror and a focusing mirror at the top of the combustion chamber, which can convert the horizontal laser beam emitted by the laser into a vertical laser beam. This ensures that the vertical laser beam can accurately irradiate the surface of the propellant specimen and allows for adjustment of the laser beam diameter. Observation windows are installed around the combustion chamber, and a laser incidence window is located at the top. The combustion chamber is a cylindrical container with a diameter of Φ88 mm and a height of 160 mm. The combustion chamber is fixed on a support frame, and the level of the combustion chamber can be adjusted by the four corners of the support frame. There are intake and pressure relief holes between the base and the observation windows, which are used to change the gas environment and pressure inside the combustion chamber. Observation windows measuring 60 mm × 120 mm are installed around the combustion chamber, and a Φ25 mm × 5 mm zinc selenide laser incidence window is mounted on the top of the combustion chamber to ensure the laboratory's sealing and the incidence of ignition laser. A pressure sensor is installed on the top cover to detect changes in pressure inside the combustion chamber. The propellant is loaded into the combustion chamber through a screw mechanism at the bottom of the chamber. The maximum pressure that the high-pressure combustion chamber can withstand is 10 MPa. Additionally, a collection plate for collecting combustion products is installed at the bottom of the combustion chamber. The center of the collection plate has a Φ8 mm circular hole, which can pass through the cylindrical support base to completely cover the bottom of the combustion chamber.

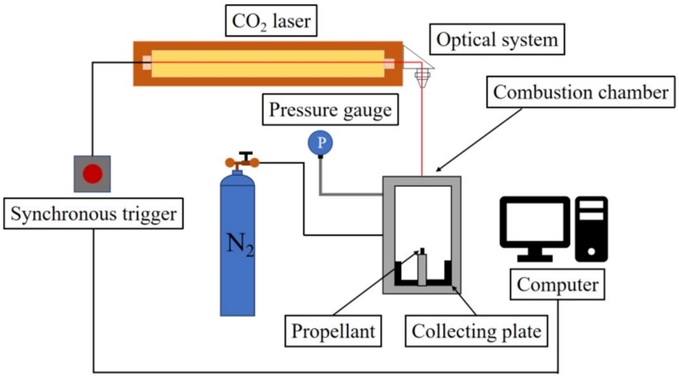

Figure 2. Schematic of the experimental apparatus.

Experimental method

The experiment is carried out at room temperature (25 ℃), the laser loading time is 1 s. After adjusting the light path and the laser ignition control system, the specimen are fixed together using positioning bolt around the center hole under the combustion chamber, and the bolts are tightened to ensure the airtightness of the combustion chamber. The pressure in the combustion chamber is adjusted using the high-pressure cylinders, and the ambient pressure in the combustion chamber is detected by the pressure sensor to meet the experimental requirements. After the flame is extinguished, discharging the gas in the combustion chamber.

Product analysis

The chemical and microscopic morphology information of CCPS is obtained from a Hitachi S-4800 scanning electron microscope (SEM) images along with X-ray energy dispersive spectrometer (EDS). The agglomeration size is measured by laser scattering particle analyzer (Mastersizer 2000). The sample quality is about 0.1 g for measuring the particle size distribution. The turbidity is kept between 10 and 20% in order to obtain accurate particle size distribution data.

Results and discussion

Analysis of the microscopic morphology of CCPs

A collecting plate is placed in the combustion chamber to collect CCPs, and then S-4800 SEM and EDS are used to analyze the microstructure of the CCPs. According to the differences in the morphology of CCPs, they can be divided into the following categories:

(1) Spherical agglomerates, as shown in Fig. 3. The agglomerate exhibit good spherical shape with a particle size of approximately 380 μm, and is widely distributed in the CCPs of containing aluminum propellant[35]. They are typical products formed by the agglomeration of aluminum particles. Analysis of the agglomerates using an Energy Dispersive X-ray Spectrometer (EDS) reveals that the interior of the agglomerates mainly consists of aluminum, oxygen, nitrogen, and carbon, with mass fractions of 50.29%, 24.90%, 16.68%, and 5.62% respectively. It can be observed that the surface of the agglomerates is primarily composed of aluminum oxide.

(2) The broken aggregates, as shown in Fig. 4. During the agglomeration process of aluminum particles, liquid aluminum gradually merges together to form molten droplets, and a hard aluminum oxide shell is formed

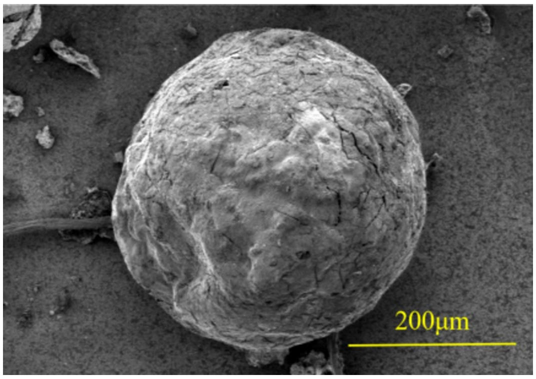

Figure 3. SEM image of a spherical agglomerate.

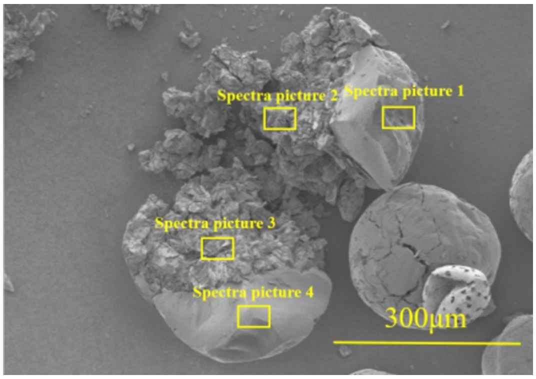

Figure 4. SEM image of broken agglomerate.

on the surface of the droplets. With the heating from the diffusion flame, the expansion coefficient of liquid aluminum is larger than that of the aluminum oxide shell, causing the liquid aluminum to expand when heated and leading to the rupture of the aluminum oxide shell[36]. As shown in Fig. 4, the internal structure of the broken agglomerate exhibits irregular patterns. Using an Energy Dispersive X-ray Spectrometer (EDS) to analyze the composition of the agglomerate at different positions, shown in Table 2. The elemental compositions of spectra picture 1 and spectra picture 4 are similar, with the ratio of aluminum to oxygen being close to each other, totaling about 70%. The nitrogen and carbon content is relatively low, indicating that position 1 and position 4 are mainly composed of aluminum oxide. On the other hand, the aluminum content in position 2 and position 3 exceeds 50%, with oxygen content around 30%, suggesting that position 2 and position 3 are primarily composed of aluminum, thereby demonstrating that the interior of the aluminum agglomerate is mainly made up of liquid aluminum.

(3) Connected aluminum aggregates, as shown in Fig. 5. The diameter of the left agglomerate is approximately 225 µm, while the diameter of the right agglomerate is approximately 256 µm. The formation of these agglomerates may have occurred when the temperature of the burning flame decreased before they completed their fusion, causing the aluminum oxide shells between them to not melt due to insufficient heat. As a result, the agglomeration process was interrupted, and after cooling down, these types of agglomerates were formed.

(4) Aluminum oxide particles,as shown in Fig. 6. The combustion products of aluminum oxide particles are dispersed at varying heights, have smooth surfaces, typically appear in clusters, and exhibit relatively complete spherical shapes with sizes not exceeding 2 µm. During the agglomeration process of aluminum

No	Al/wt%	O/wt%	N/wt%	C/wt%
1	40.64	30.52	15.65	13.19
2	55.32	31.14	4.23	9.31
3	54.28	31.28	4.44	10.00
4	37.12	36.11	12.76	7.96

Table 2. composition of CCPs.

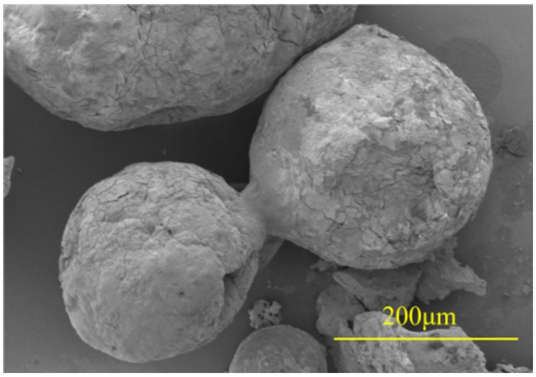

Figure 5. SEM image of two agglomerates connected.

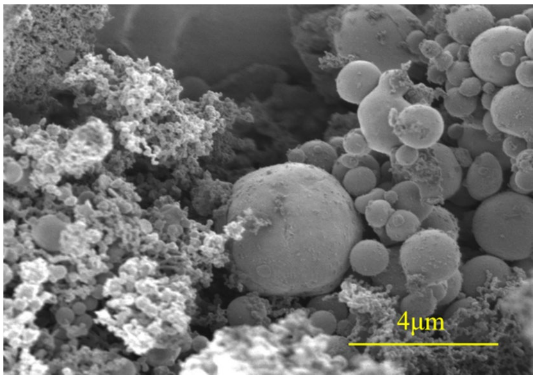

Figure 6. SEM image of alumina particle.

particles, micron-sized aluminum particles first vaporize and evaporate into aluminum vapor under the heating of the diffusion flame, which then reacts with oxygen in the environment. Some of the oxidized products of aluminum vapor condense on the surface of aluminum droplets to form oxide cap structures, while the rest of the aluminum vapor condenses directly in the environment to form submicron or even nanoscale aluminum oxide particles[37,38].

Microstructure of condensed combustion products of different formulations propellant

In order to investigate the microstructure of condensed combustion products from different formulations of NEPE propellants, electron scanning microscopy was used to observe the solid combustion products from four NEPE propellant formulations (JF-1, JF-2, JF-3, and JF-4) at 3 MPa and 7 MPa, as shown in Figs. 7, 8, 9,10. It can be seen that the condensed combustion products of these four NEPE propellant formulations are mainly composed of spherical aluminum agglomerates and irregularly shaped carbon agglomerates. At 3 MPa, the spherical

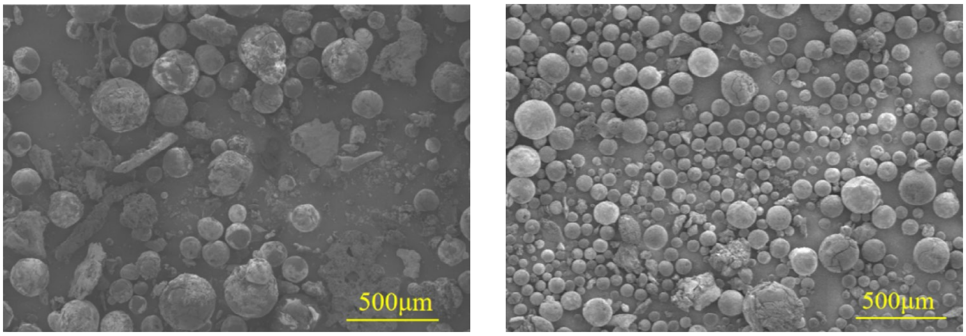

(a)3MPa (b)7MPa

Figure 7. SEM images of the condensed combustion products of JF-1 propellant.

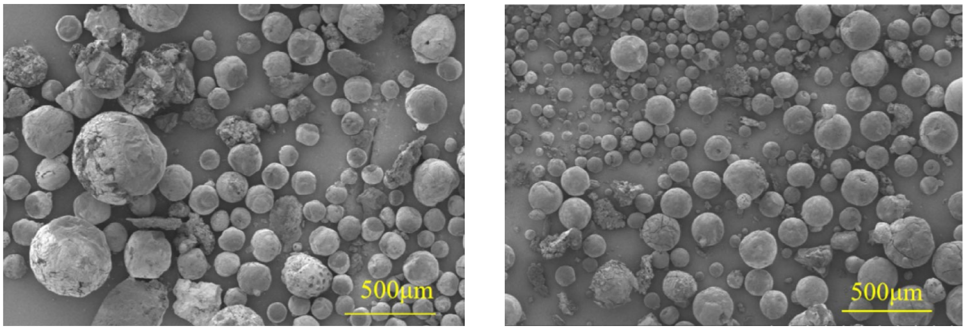

(a)3MPa (b)7MPa

Figure 8. SEM images of the condensed combustion products of JF-2 propellant.

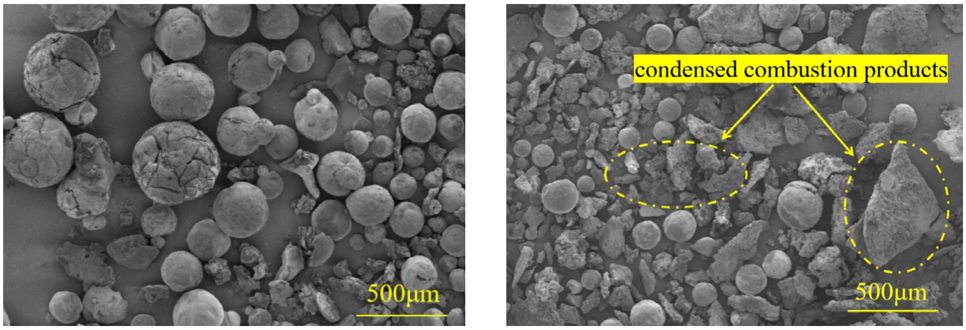

(a)3MPa (b)7MPa

Figure 9. SEM images of the condensed combustion products of JF-3 propellant.

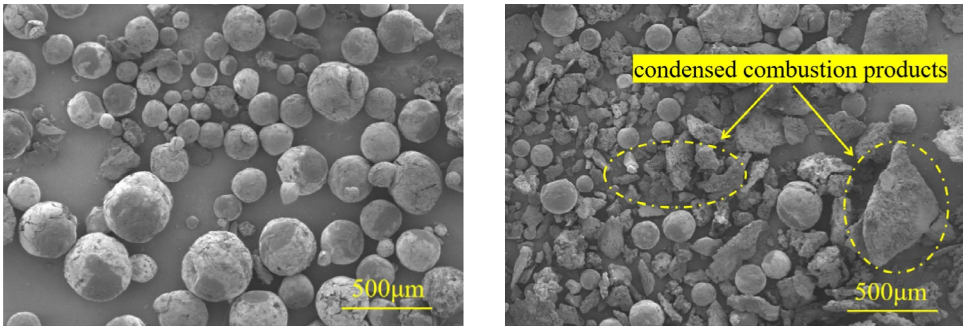

(a)3MPa (b)7MPa

Figure 10. SEM images of the condensed combustion products of JF-4 propellant.

aluminum agglomerates in the condensed combustion products of these four NEPE propellant formulations have larger sizes, and the agglomerates' shells exhibit irregular spherical structures. Additionally, more aluminum agglomerates with broken shells can be observed in the condensed combustion products. At 7 MPa, the size of the spherical aluminum agglomerates in the condensed combustion products decreases compared to 3 MPa. The agglomerates' shells become smoother, and the spherical shape becomes more perfect. In the condensed combustion products at 7 MPa for JF-3 and JF-4, a large number of carbon agglomerates were found. This may be due to the increased particle size of AP, which leads to uneven heat transfer within the propellant composition and incomplete combustion of components with high carbon content such as binders and plasticizers. Moreover, the excessive burning rate in the high-pressure environment could cause insufficient combustion of the binder and plasticizer. However, due to the limitations of scanning electron microscope images, it is difficult to determine the influence of propellant formulations on the size of condensed combustion products based solely on the microstructure of the four NEPE propellant formulations. Further quantitative analysis of the particle size of condensed combustion products is needed.

Crystal phase composition analysis of condensate combustion products

To investigate the combustion reaction mechanism of NEPE propellants and determine the changes in surface crystal structure of solid combustion products, X-ray diffractometry was employed to analyze the CCPs of JF-1, JF-2, JF-3, and JF-4 propellant at 3 MPa. Figure 11 shows the the diffraction patterns of the CCPs of the four propellants. Compared with the standard card, the CCPs of the four propellant samples mainly contain Al_2O_3 and Al. The aluminum particles burned to form α-Al_2O_3 and γ-Al_2O_3, indicating that under the current experimental conditions, the aluminum particles did not burn completely.

According to Fig. 11, it can be observed that as the particle size of Al increases, the intensity of the Al diffraction peak also increases. This indicates a decrease in the relative content of Al_2O_3 in the solid combustion products with an increase in the particle size of Al in the samples. Finer Al particles have higher reactivity, allowing them to generate a higher concentration of oxidizing gas in a given time and promote the combustion

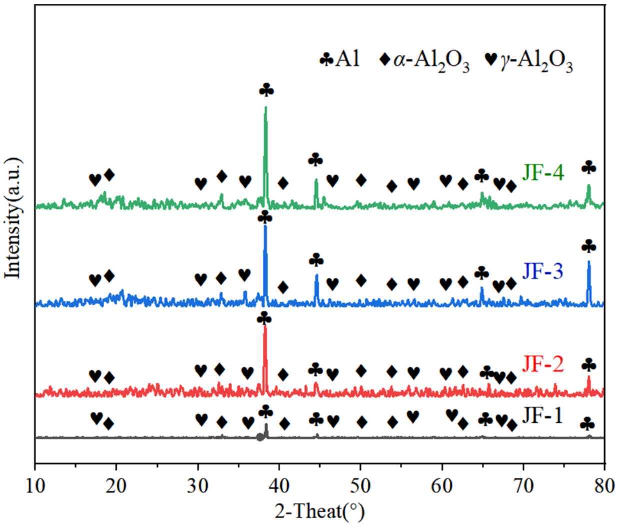

Figure 11. XRD patterns of the CCPs of NEPE propellants with different formulations.

of Al particles. Furthermore, with an increase in the particle size of AP, the intensity of the Al diffraction peak gradually increases, while the intensity of the Al_2O_3 diffraction peak slightly decreases. This suggests an increase in the relative content of Al in the CCPs with an increase in AP particle size. This is because smaller AP particles have higher reactivity, resulting in a lower concentration of oxidizing gas generated in a given time, thereby suppressing the combustion of Al particles.

Particle size analysis of the CCPs

In order to study the particle size distribution of the CCPs from different formulations of NEPE propellants, the CCPs were collected by combustion experiments at 1 MPa and 3 MPa for JF-1, JF-2, JF-3, and JF-4 propellant. The particle size distribution of the CCPs was analyzed using a laser particle analyzer within a range of 0.01–1000 μm.

Due to the fact that the initial particle size of aluminum in propellants is not a fixed value but rather a range of particle sizes, it can lead to situations where the diameter of individual aluminum particles is similar to or the same as the diameter of small-sized initial aggregates. This makes it difficult to distinguish whether the particles are unaggregated aluminum particles or small-sized initial aggregates[31]. Therefore, it is necessary to define a cutoff diameter for aggregates, denoted as D_{cut}. Only when the particle diameter on the burning surface of the propellant is larger than Dcut, it will be considered as an aggregate. Particles with diameters smaller than D_{cut} are regarded as individual aluminum particles that have not undergone the aggregation process. The studies conducted by Sambamurthi[7], Jackson[31], and Gallier[33], all utilized the parameter (D_{cut}) for aggregates to differentiate whether the particles on the burning surface are aggregates or not. The cutoff diameter for aggregates is related to the initial average particle size of aluminum in the propellant[12].

The particle size distribution of the at 1 MPa of JF-1 propellant is shown in Fig. 12, and the particle size measurement results are presented in Table 3. From Fig. 8, the particle size distribution of all particles in the solid combustion products can be observed, including the unaggregated aluminum particles on the burning surface of the propellant (particles with a diameter smaller than D_{cut}). The entire particle size distribution of the CCPs from the JF-1 propellant follows a log-normal distribution. The peak of the percentage of particle count is in the diameter range of 144–211 μm, accounting for 56.61% of the total number of particles. It is worth noting that the initial particle size of aluminum in the JF-1 propellant is 3 μm, whereas only 10% of the particles in the solid combustion products have a diameter smaller than 145 μm. This indicates that under the experimental conditions, there is significant aggregation of aluminum particles in the NEPE propellant.

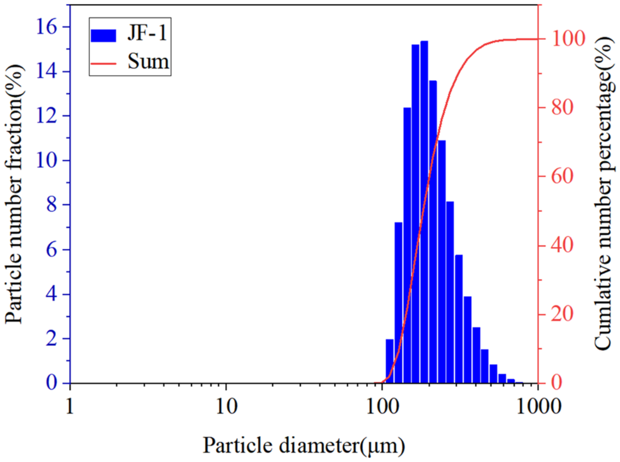

Figure 12. Particle size distribution of CCPs at 1 MPa of JF-1 propellant.

Sample	Pressure	d(0.1)	d(0.5)	d(0.9)
JF-1	1 MPa	145	207	347
JF-2	1 MPa	144	202	322
JF-3	1 MPa	12.3	17.7	30.3
JF-4	1 MPa	3.8	5.05	11.6
JF-1	3 MPa	74.8	132	245
JF-2	3 MPa	49.5	69.5	125
JF-3	3 MPa	4.48	6.08	10.6
JF-4	3 MPa	3.36	4.63	8.82

Table 3. Size distribution of the CCPs of NEPE propellants of different formulations (μm).

The particle size distribution of the CCPs at 1 MPa of JF-1 propellant is shown in Fig. 13, and the particle size measurement results are shown in Table 3. For JF-1 propellant, the particle size distribution of condensed phase combustion products at 3 MPa is also roughly normal. The peak curve of particle number percentage ranges from 86.4 µm to 186 µm, and d(0.5) is 132 µm, which is 36.2% lower than that at 1 MPa. It can be seen that the agglomeration degree of JF-1 propellant during combustion at 3 MPa is lower than that at 1 MPa.

Figure 14 shows the particle size distribution of the CCPs of JF-2 propellant at 1 MPa, and the particle size measurement results are shown in Table 3. The particle size distribution of the condensed combustion product of JF-2 propellant under 1 MPa is similar to that of JF-1 propellant. The total number of particles of JF-2 propellant in the diameter range of 144–211 µm is 59.35%, and the peak value of particle distribution is also very close to that of JF-1 propellant, but the initial particle size of aluminum particles of SP-3 propellant is 30 µm. Therefore, it can be seen that although the particle size distribution of the CCPs of the two groups of NEPE propellants is similar, the agglomeration degree of the aluminum particles of the CCPs of JF-1 propellants is higher.

Figure 15 shows the particle size distribution of the CCPs at 3 MPa of JF-2 propellant, and the particle size measurement results are shown in Table 3. The peak curve of JF-2 propellant particle number percentage is located in the range of 45.6–86.4 µm, and d(0.5) is reduced by 65.6% compared with that in 1 MPa, and 47.3% compared with that in JF-1 propellant. It can be seen that when the initial particle size of Al particles in NEPE propellant increases from 3 to 30 µm, the degree of aluminum agglomeration decreases under high pressure. This may be caused by the large difference between the burning rate of the two propellants when $p = 3$ MPa, while the burning rate of JF-1 propellants is not much different from that of JF-2 propellants at 1 MPa, and the initial aluminum particle size of JF-2 propellants is larger, which makes it easier to form large-sized aggregates. The particle size distribution of the CCPs of the two propellants at 3 MPa is similar.

According to the aluminum agglomeration pocket model[3], the Al particles within the propellant are located within the "pockets" formed by AP particles. When the AP particle size in the propellant remains constant, the size of the pockets formed by AP also remains constant. Therefore, as the particle size of Al decreases in the

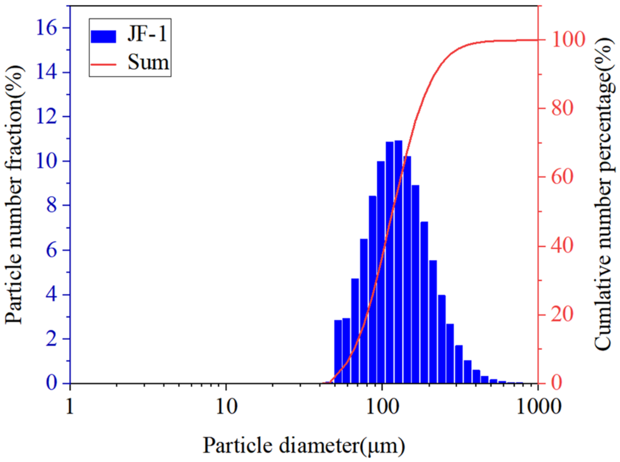

Figure 13. Particle size distribution of the CCPs at 3 MPa of JF-1 propellant.

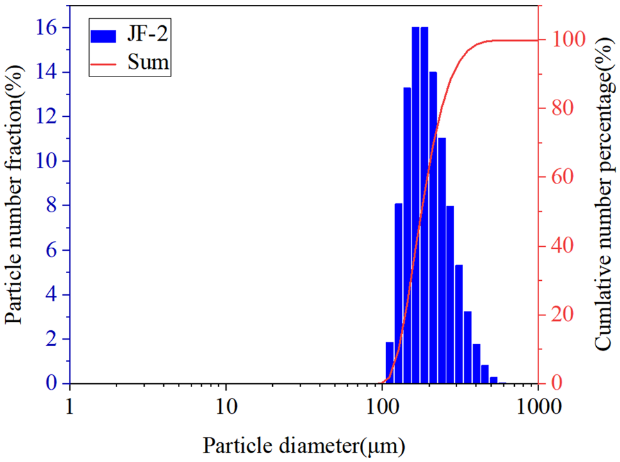

Figure 14. Particle size distribution of the CCPs at 1 MPa of JF-2 propellant.

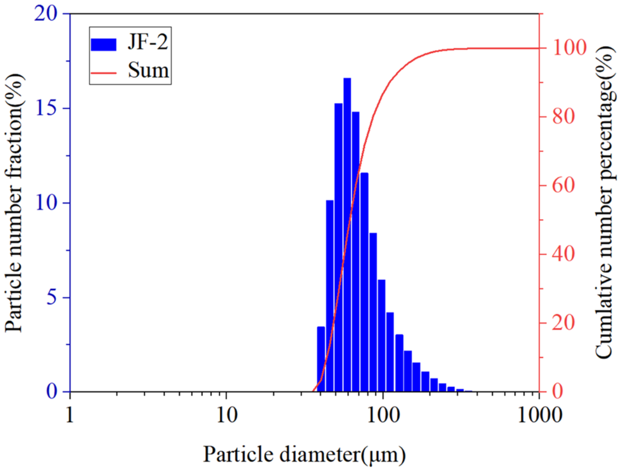

Figure 15. Particle size distribution of the CCPs at 3 MPa of JF-2 propellant.

propellant, the concentration of Al within the pockets increases, leading to the formation of larger aluminum aggregates and more pronounced agglomeration phenomena. On the other hand, smaller-sized Al particles possess higher reactivity and exhibit better compatibility with AP in the propellant. Under the same experimental conditions, NEPE propellants containing smaller-sized Al particles exhibit higher thermal conductivity efficiency within their systems. This results in a stronger thermal reaction and an increased release of heat during the combustion reaction. Consequently, a greater number of Al particles undergo shell rupture due to phase transition under the effect of thermal feedback. Simultaneously, more adjacent ruptured Al particles experience agglomeration phenomena. As a result, the degree of agglomeration is higher, leading to an increase in the size of the solid combustion products after combustion.

The particle size distribution of the CCPs at 1 MPa of JF-3 and JF-4 propellants is shown in Figs. 16 and 17, and the particle size measurement results are presented in Table 3. The percentage of particle count peaks for the solid combustion products of both JF-3 and JF-4 propellants follow a normal distribution. For JF-3 propellant, the peak of the percentage of particle count is in the diameter range of 11.2–21.2 μm, accounting for 76.08% of the total number of particles. Among them, 50% of the particles have a diameter smaller than 17.7 μm, which is a 91.5% decrease compared to the d(0.5) value of JF-1 propellant. For JF-4 propellant, the peak of the percentage of particle count is in the diameter range of 4.03–7.64 μm, accounting for 81.68% of the total number of particles. Among them, 50% of the particles have a diameter smaller than 5.05 μm, which is a 97.6% decrease compared to the d(0.5) value of JF-1 propellant. It's worth noting that JF-1, JF-3, and JF-4 propellants all have an initial particle size of 3 μm for Al particles. Under the experimental conditions, as the particle size of AP particles in the NEPE propellant increases from 200–300 μm to 300–400 μm and 400–500 μm, the particle diameter distribution of the CCPs gradually decreases, and the degree of Al particle agglomeration decreases. When the AP particle size is in the range of 400–00 μm, the reduction in the peak of the particle size distribution for the is particularly significant compared to NEPE propellant containing 200–300 μm AP particles.

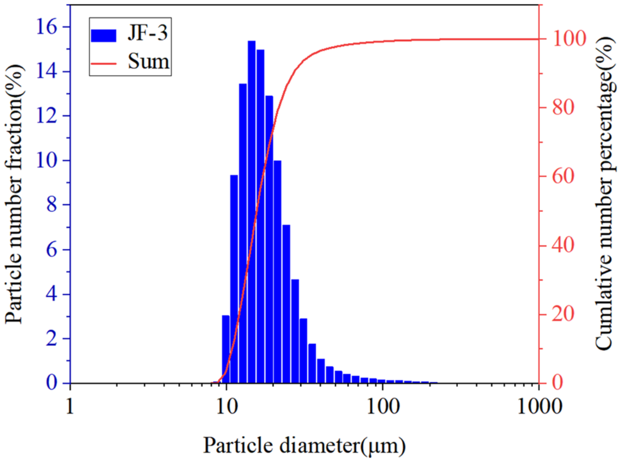

Figure 16. Particle size distribution of the CCPs at 1 MPa of JF-3 propellant.

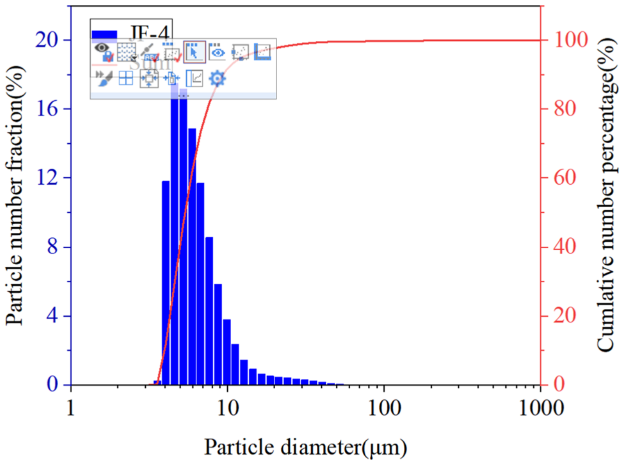

Figure 17. Particle size distribution of the CCPs at 1 MPa of JF-4 propellant.

The particle size distribution of the CCPs at 3 MPa of JF-3 propellant and JF-4 propellant is shown in Figs. 18 and 19, and the particle size measurement results are presented in Table 3. For JF-3 propellant, the peak of the percentage of particle count is in the diameter range of 4.03–7.64 μm, accounting for 81.68% of the total number of particles. This represents a 95.4% decrease compared to the d(0.5) value of JF-1 propellant. For JF-4 propellant, the peak of the percentage of particle count is in the diameter range of 3.12–5.92 μm, accounting for 79.66% of the total number of particles. This represents a 96.5% decrease compared to the d(0.5) value of JF-1 propellant. It can be observed that the degree of agglomeration for JF-3 propellant and JF-4 propellants at 3 MPa is lower compared to that at 1 MPa. Additionally, increasing the size of AP particles leads to a decrease in Al agglomeration in NEPE propellants.

With the increase of AP particle size in the propellant, the burning rate of AP/Al, an important component of NEPE propellant, will be increased, and the stay time of aluminum particles on the propellant combustion surface will be reduced. Meanwhile, the heating time of Al particles will be shortened, so the melting degree of Al particles and the rupture of the oxide film on the surface of Al particles will be reduced. As a result, a relatively small number of Al particles adhere to each other to form smaller agglomerated particles. On the other hand, AP particles with smaller particle size have larger specific surface area and higher reactivity, so AP particles with smaller particle size can decompose and produce higher product concentration per unit time, and the increased product concentration can increase the contact area between oxidizing gas products and unburned Al particles and Al vapor, so the degree of combustion reaction becomes stronger and the heat release increases. The increase of heat release further accelerates the rupture of the Al_2O_3 shell on the surface of Al particles, exposing more molten Al elements in the oxidation shell of Al particles, increasing the contact chance between adjacent Al particles, and eventually forming larger sized agglomerated particles. Therefore, the increase of AP particle size in NEPE propellants will reduce the particle size of the CCPs to a certain extent.

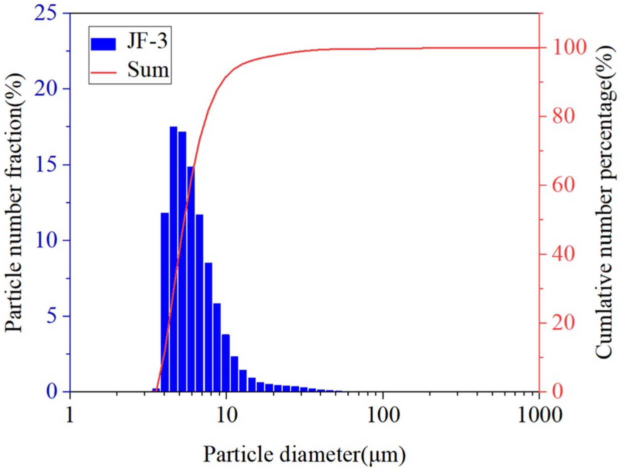

Figure 18. Particle size distribution of the CCPs at 3 MPa of JF-3 propellant.

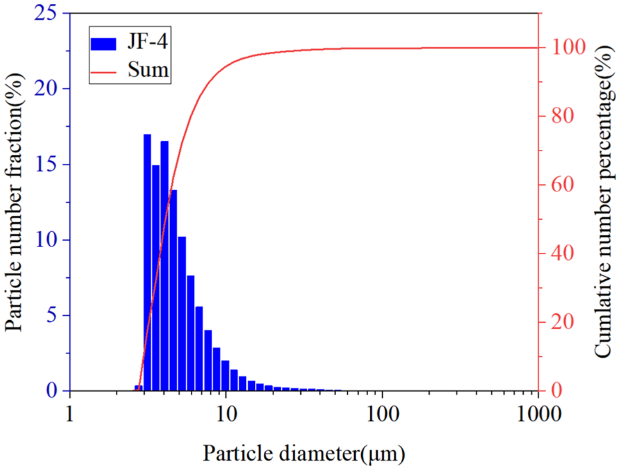

Figure 19. Particle size distribution of the CCPs at 3 MPa of JF-4 propellant.

Al agglomeration model

The combustion process of solid propellants is highly complex, and the microstructure and combustion environment have a significant impact on the combustion of Al particles. Therefore, it is challenging to accurately describe the physical processes of Al particle agglomeration and fusion between agglomerates using mathematical models. In early research, various models were proposed to describe the agglomeration behavior of Al particles in solid propellants, including empirical models[12,26–28], pocket models[29–31], physical models[32–34], and random packing models[24,25]. Among them, the pocket model has gained more attention due to its simplicity and reasonable description of agglomerate properties. The main concept of the pocket model is that the region between adjacent AP particles forms a "pocket" where all the Al particles agglomerate on the burning surface to form an agglomerate. The pocket model can provide good predictions of agglomerate size. However, the pocket model is still limited by its assumption of an imprecise propellant structure, which reduces its reliability. Therefore, further research is necessary to improve the agglomeration models for particles.

The establishment of Al agglomeration model

By performing electron microscopy scanning on the solid propellant surface, the distribution of AP particles on multiple surfaces can be obtained. Figure 20 shows the SEM image of AP distribution on the surface of SP-2 propellant. In the agglomeration model discussed in this section, the distance D between adjacent AP particles in the two-dimensional SEM image is approximated as the size of the three-dimensional "pocket" region. Figure 21 illustrates the concept of the pocket model, where the circular region surrounded by adjacent AP particles is considered as the pocket range in this model. The distance D between AP particles is approximated as the size of the pocket. Within the pocket, Al particles and ammonium nitrate explosive are encapsulated, and the aluminum particles contained in the pocket undergo agglomeration during the combustion process to form aluminum agglomerates. Through SEM images of the propellant surface, the distance between AP particles can be obtained. In Fig. 16, spherical-shaped AP particles and hemispherical pits with diameters similar to AP can

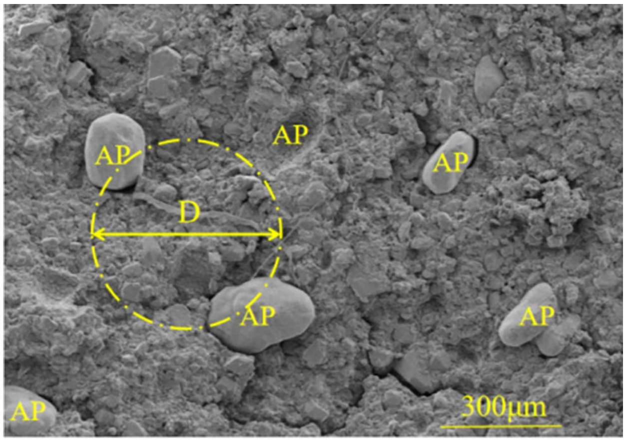

Figure 20. SEM diagram of AP distribution on SP-2 propellant surface.

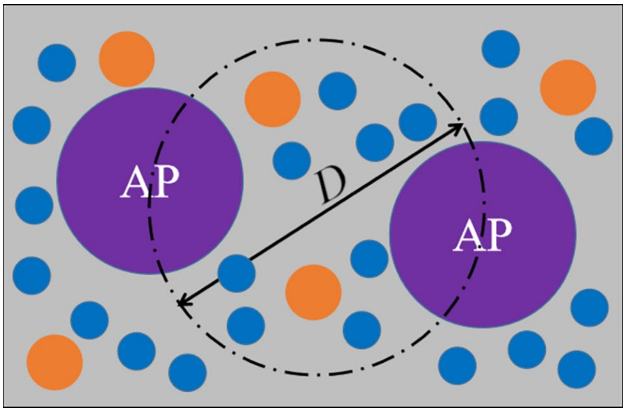

Figure 21. Schematic diagram of the pocket model.

be clearly observed. These pits are formed when a propellant specimen is cut, and some AP particles are taken away by the other half of the propellant surface, leaving behind on the propellant surface. When calculating the pocket diameter, these pit locations also represent AP particles, allowing for a more accurate estimation of the pocket size based on the actual situation.

Due to the fact that the distance D between adjacent AP particles measured from the SEM image of the propellant includes a portion of the AP particles, the actual diameter D_{pocket} of the pocket should be smaller than D. In this paper, according to the reference[17], the measured diameter D is multiplied by a correction factor γ, so D_{pocket} can be expressed as:

$$D_{\text{pocket}} = \gamma D \tag{1}$$

where γ is the correction factor introduced to consider the spatial influence of AP particles within the diameter range D_{pocket}[39]. The value of γ is related to the diameter D_{pocket} of the pocket and the diameter D_{AP} of the AP particles. As D increases and D_{AP} decreases, γ approaches 1, indicating a higher spatial occupancy of AP particles within the pocket. Conversely, when D_{pocket} is smaller and D_{AP} is larger, γ approaches 0, indicating a lower spatial occupancy of AP particles within the pocket. So γ can be expressed as:

$$\gamma = (1 - Y_{\text{AP}})^{1/3} \tag{2}$$

where Y_{AP} is the volume fraction of AP particles.

In JF-2 propellant, according to the mass fraction and density of AP, Al, CL-20 and HMX, the volume fraction of each component in the propellant can be calculated as follows:

$$Y_{\text{AP}} = \frac{\varepsilon_{\text{AP}} \times \rho_{\text{P}}}{\rho_{\text{AP}}} \tag{3}$$

$$Y_{\text{Al}} = \frac{\varepsilon_{\text{Al}} \times \rho_{\text{P}}}{\rho_{\text{Al}}} \tag{4}$$

$$Y_{\text{CL - 20}} = \frac{\varepsilon_{\text{CL - 20}} \times \rho_{\text{P}}}{\rho_{\text{CL - 20}}} \tag{5}$$

$$Y_{\text{HMX}} = \frac{\varepsilon_{\text{HMX}} \times \rho_{\text{P}}}{\rho_{\text{HMX}}} \tag{6}$$

where ε_{AP}, ε_{Al}, ε_{HMX} and $\varepsilon_{\text{CL-20}}$ are the mass fractions of each component, and ρ_{AP}, ρ_{Al}, ρ_{HMX}, $\rho_{\text{CL-20}}$ and ρ_{p} are the densities of each component and the propellant, respectively.

If the region between adjacent AP particles is considered as the pocket range, and the pockets only contain Al, HMX, and CL-20, assuming that the Al, HMX, and CL-20 particles within the pocket region are uniformly distributed with plasticizers and binders filling the space between them, without considering the randomness of Al, HMX, and CL-20 particles, then the volume fractions of Al, HMX, and CL-20 particles in each pocket region can be expressed as:

$$Y_{\text{pocket,Al}} = \frac{Y_{\text{Al}}}{1 - Y_{\text{AP}}} \tag{7}$$

$$Y_{\text{pocket,HMX}} = \frac{Y_{\text{HMX}}}{1 - Y_{\text{AP}}} \tag{8}$$

$$Y_{\text{pocket,CL - 20}} = \frac{Y_{\text{CL - 20}}}{1 - Y_{\text{AP}}} \tag{9}$$

According to Eqs. (7), (8) and (9), the number of HMX, CL-20 and Al particles in each pocket can be expressed as follows:

$$N_{\text{HMX}} = \frac{D^3_{\text{pocket}} \times Y_{\text{pocket,HMX}}}{D^3_{\text{HMX}}} \tag{10}$$

$$N_{\text{CL - 20}} = \frac{D^3_{\text{pocket}} \times Y_{\text{pocket,CL - 20}}}{D^3_{\text{CL - 20}}} \tag{11}$$

$$N_{\text{Al}} = \frac{(D^3_{\text{pocket}} - D^3_{\text{HMX}} \times N_{\text{HMX}} - D^3_{\text{CL - 20}} \times N_{\text{CL - 20}})Y_{\text{pocket,Al}}}{D^3_{\text{Al}}} \tag{12}$$

where D_{HMX}, $D_{\text{CL-20}}$ and D_{Al} represent the average particle size of HMX, CL-20 and Al particles in the propellant.

Therefore, the total mass of aluminum particles within each pocket range can be expressed as:

$$m_{\text{Al}} = N_{\text{Al}} \times \frac{\pi}{6} \times D^3_{\text{Al}} \times \rho_{\text{Al}} \tag{13}$$

Assuming that all the aluminum particles contained in the pocket only aggregate to form a larger aggregate, the aggregate particle diameter D_{agg} formed is:

$$D_{\text{agg}} = \left(\frac{6 \times m_{\text{Al}}}{\pi \times \rho_{\text{Al,l}}}\right)^{\frac{1}{3}} \tag{14}$$

where $\rho_{\text{Al,l}}$ is the density of liquid aluminum, 2.35×10^3 kg/m^3. It can be seen from previous studies that the interior of the aluminum aggregate is composed of liquid aluminum[19].

In previous studies, it was found that the burning rate of propellant is one of the important factors influencing aluminum agglomeration[40]. Therefore, in this section's model, the influence of burning rate on agglomeration needs to be considered. The empirical estimate of burning rate in the empirical model proposed by Duterque[28] is $2.42/\dot{r}$. While Liu[11] provided an empirical estimation for the burning rate:$2.69/\dot{r}$. Due to the complexity of the agglomeration model and the lack of a precise mathematical model for the effect of burning rate on agglomerate particle size, fitting mathematical models can be obtained by collecting a large amount of experimental data, which are reasonably accurate. In this paper, adopting the modified burning rate coefficient method proposed by Duterque[22], and considering the influence of combustion process on agglomeration process. The modified aggregate diameter can be expressed as:

$$D_{\text{agg,1}} = (2.24/\dot{r})D_{\text{agg}} \tag{15}$$

After the initial aggregate is formed and until it is removed from the propellant burning surface, multiple aggregates usually come close to each other and fuse to form larger aggregates. After taking this factor into account, it is introduced into the model. In order to facilitate calculation, coefficient a is added as the influence factor. Assuming that the initial aggregate i and the aggregate j undergo a secondary agglomeration, the size of the new aggregate formed can be expressed as:

$$D_{agg,2} = a^3\sqrt{\left(D_{agg,1,i}\right)^3 + \left(D_{agg,1,j}\right)^3} \tag{16}$$

where a is the coefficient, which is affected by the agglomeration physical process, such as the process of merging three or more aggregates on the propellant burning surface, or further growth near the propellant surface before ejection, etc. For different solid propellants, the value of a is different. In this study, the value of a is 1.25.

In order to facilitate calculation, assuming that the sizes of the two aluminum aggregates that undergo secondary agglomeration are equal, the size of the new agglomeration after secondary agglomeration can be expressed as:

$$D_{agg,2} = a^3\sqrt{2\left(D_{agg,1}\right)^3} \tag{17}$$

In summary, the initial size of aluminum agglomerates on the propellant combustion surface and the size of new agglomerates after secondary agglomerations can be predicted according to Eqs. (15) and (17).

The verification of Al agglomeration model

In this section, the test data of JF-1 propellant are compared with that of the prediction model to verify the reasonableness of the model. The relevant parameters of JF-1 propellant are shown in Table 4. Under the conditions of 1–8 MPa, the experimentally measured burning rate is shown in Table 5, and it can be seen that the burning rate increases as the pressure increases. As the pressure increases, the surface convective heat flux and the

Parameter	Value
ρ_{AP}	1.95×10^3 kg/m^3
ρ_{Al}	2.7×10^3 kg/m^3
ρ_P	1.86×10^3 kg/m^3
$\rho_{Al,l}$	2.35×10^3 kg/m^3
ρ_{HMX}	1.96×10^3 kg/m^3
$\rho_{CL\text{-}20}$	2.61×10^3 kg/m^3
D	350 μm

Table 4. Related parameters of JF-1 propellant.

p/MPa	1.0	2.0	3.0	5.0	7.0	8.0
$\dot{r}/(\mathrm{mm}\cdot\mathrm{s}^{-1})$	3.66	5.51	7.14	9.62	11.83	13.28

Table 5. The burning rate of SP-2 propellant under different pressures.

radiant heat flux increase, resulting in an increase of the burning[41]. The agglomeration size model of propellant was calculated under 1.0–8.0 MPa.

In order to verify the reliability of the agglomeration size model established in this paper, the prediction results of the earlier empirical model and the pocket model are compared with the model proposed in this paper.

Empirical model proposed by Salita[23]:

$$D_{\mathrm{Sa}} = \frac{869}{r(Y_{\mathrm{AP}} + Y_{\mathrm{Al}})^2} \tag{18}$$

Empirical model proposed by Liu[11]:

$$D_{\mathrm{Liu}} = \frac{2690(Y_{\mathrm{Al}} + Y_{\mathrm{RDX}} + 1)}{r(Y_{\mathrm{Al}} + Y_{\mathrm{RDX}})\left(\frac{D_{\mathrm{Al}}}{50} + 1\right)} \tag{19}$$

Pocket model proposed by Cohen[12]:

$$D_{\mathrm{Cohen}} = \left(\frac{\rho_{\mathrm{AP}} Y_{\mathrm{Al}}}{\rho_{\mathrm{Al}} Y_{\mathrm{AP}}}\right)^{\frac{1}{3}} D_{\mathrm{AP}} \tag{20}$$

Based on Cohen pocket model, Duterque[28] proposed a rule of influence of combustion rate on agglomeration size, which can be expressed as:

$$D_{\mathrm{Duterque}} = \frac{2.42}{r} D_{\mathrm{Cohen}} + 80.26 \tag{21}$$

To validate the reliability of the agglomeration model proposed in this paper, the empirical models proposed by Salita and Duterque were compared with the $D_{\mathrm{agg},1}$ model and the $D_{\mathrm{agg},2}$ model. Figure 22 shows the comparison between experimental results and different agglomeration models.

From Fig. 22, it can be seen that the predicted values of the $D_{\mathrm{agg},1}$ model are closer to the results of the empirical model and the pocket model compared to the experimental measurements. However, there is a significant difference between the predicted values and the experimental measurements. On the other hand, the predicted agglomerate size from the $D_{\mathrm{agg},2}$ model shows better agreement with the experimental values, with a relative error within 10%. This may be attributed to the significant occurrence of secondary agglomeration in the aluminum agglomerates of the propellant being studied, which is not considered in the empirical model proposed by Salita and the pocket model proposed by Duterque. As a result, the predicted values of these two models are closer to the predictions of the $D_{\mathrm{agg},1}$ model. This further confirms that the secondary agglomeration prediction model ($D_{\mathrm{agg},2}$ model) provides a more reasonable description of aluminum agglomeration in the NEPE propellant used in this experiment. It can accurately predict the size of aluminum agglomerates in the NEPE propellant.

Conclusions

This paper investigates the physicochemical properties of the CCPs of aluminized NEPE propellants. The microstructure of the CCPs is analyzed using scanning electron microscopy (SEM), and based on their morphology, they are classified and studied for NEPE propellant with different formulations. The crystal phase composition of the CCPs for different propellant is analyzed using X-ray diffraction (XRD). Furthermore, the particle size distribution characteristics of the CCPs under different conditions and for different propellant are studied using a laser particle size analyzer. The main conclusions are summarized as follows:

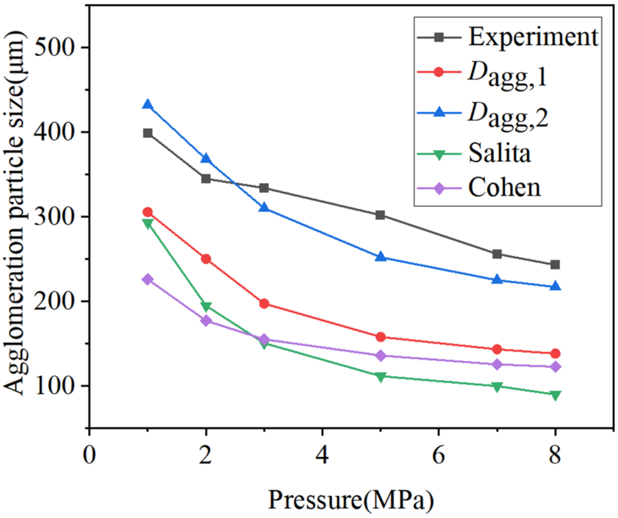

Figure 22. Experimental and model calculation values of agglomerate size.

(1) The condensed combustion products of aluminized NEPE propellant mainly consist of aluminum agglomerates and oxide particles. According to the morphology of aluminum agglomerates, they can be classified into three categories, which are closely related to the combustion process of aluminum particles on the burning surface of the propellant. The particle size of aluminum oxide particles typically does not exceed 2 μm.

(2) By comparing the microstructures of the CCPs of JF-1, JF-2, JF-3, and JF-4 propellants under 3 and 7 MPa, it was found that the diameter of spherical aluminum agglomerates in these four NEPE propellants is smaller at 7 MPa compared to 3 MPa. Additionally, the aluminum agglomerates have smoother outer shells and more perfect spherical shapes at 7 MPa.

(3) X-ray diffraction analysis of the CCPs of JF-1, JF-2, JF-3, and JF-4 propellants under 3 MPa revealed the presence of both Al and Al_2O_3. This indicates that under the current experimental conditions, the aluminum particles did not burn completely. The intensity of the Al diffraction peaks was found to be: JF-4 > JF-3 > JF-2 > JF-1. It can be observed that under these experimental conditions, JF-1 propellant had the highest degree of aluminum oxidation, while JF-4 propellant had the lowest degree of aluminum oxidation.

(4) The particle size of the CCPs of JF-1, JF-2, JF-3, and JF-4 propellants under 1 MPa and 3 MPa was analyzed by using a laser particle size analyzer. For the four NEPE propellants used in the study, when the particle size of Al particles increased from 3 μm to 30 μm, it showed the poorest inhibition effect on aluminum particle agglomeration. However, when the AP particle size increased to 400–500 μm, the particle size distribution of the CCPs became the smallest.

(5) Based on the agglomeration behavior of aluminum particles and the principles of the classical pocket model, a mathematical agglomeration model was proposed to predict the size of agglomerates. This model can be used to predict the size of aluminum agglomerates on the burning surface of the propellant. The experimental measurements were compared with multiple prediction models, and the results showed that the predictions from the secondary agglomeration model were closer to the experimental results.

Data availability

The datasets used during the current study available from the corresponding author on reasonable request.

Received: 11 April 2024; Accepted: 13 August 2024

References

1. Badiola, C., Gill, R. J. & Dreizin, E. L. Combustion characteristics of micron-sized aluminum particles in oxygenated environments. *Combust. Flame.* **158**(10), 2064–2070 (2011).
2. Gill, R. J., Badiola, C. & Dreizin, E. L. Combustion times and emission profiles of micron-sized aluminum particles burning in different environments. *Combust. Flame.* **157**(11), 2015–2023 (2010).
3. Mohan, S., Furet, L. & Dreizin, E. L. Aluminum particle ignition in different oxidizing environments. *Combust. Flame.* **157**(7), 1356–1363 (2010).
4. Liu, X., Ao, W., Liu, H. & Liu, P. J. Aluminum agglomeration on burning surface of NEPE propellants at 3–5MPa. *Propell. Explos. Pyrot.* **42**(3), 260–268 (2016).
5. Yuan, J., Liu, J., Zhou, Y., Wang, J. R. & Xv, T. W. Aluminum agglomeration of AP/HTPB composite propellant. *Acta Astronaut.* **156**(5), 14–22 (2019).
6. Tu, C. Y., Chen, X., Li, Y. K., Zhang, B. C. & Zhou, C. S. Experimental study of Al agglomeration on solid propellant burning surface and condensed combustion products. *Def. Technol.* **26**(8), 111–122 (2023).

7. Sambamurthi, J. K., Price, E. W. & Sigman, R. K. Aluminum agglomeration in solid-propellant combustion. *AIAA J.* **22**(8), 1132–1138 (1984).
8. Babuk, V. A., Vasilyev, V. A. & Malakhov, M. S. Condensed combustion products at the burning surface of aluminized solid propellant. *J. Propul. Power.* **15**(6), 783–793 (1999).
9. Glotov, O. G. Condensed combustion products of aluminized propellants. II. Evolution of particles from distance from the burning surface. *Combust. Eeplo. Shock.* **36**(4), 476–487 (2000).
10. Anand, K. V. *et al.* Experimental data and model predictions of aluminium agglomeration in ammonium perchlorate-based composite propellants including plateau-burning formulations. *P. Combust. Inst.* **34**(2), 2139–2146 (2013).
11. Liu, T. K. Experimental and model study of agglomeration of burning aluminized propellants. *J. Propul. Power.* **21**(5), 797–806 (2015).
12. Cohen, N. S. A pocket model for aluminum agglomeration in composite propellants. *AIAA J.* **21**(5), 72–72 (2012).
13. Babuk, V. A., Vassiliev, V. A. & Sviridov, V. V. Propellant formulation factors and metal agglomeration in combustion of aluminized solid rocket propellant. *Combust. Sci. Technol.* **163**(1), 261–289 (2001).
14. Mullen, J. C. & Brewster, M. Q. Reduced agglomeration of aluminum in wide-distribution composite propellants. *J. Propul. Power.* **27**(3), 650–661 (2015).
15. Takahashi, K., Oide, S. & Kuwahara, T. Agglomeration characteristics of aluminum particles in AP/AN composite propellants. *Propell. Explos. Pyrot.* **38**(4), 555–562 (2013).
16. Jayaraman, K., Chakravarthy, S. R. & Sarathi, R. Quench collection of nano-aluminium agglomerates from combustion of sandwiches and propellants. *Proc. Combust. Inst.* **33**(2), 1941–1947 (2011).
17 Glotov, O. G. Condensed combustion products of aluminized propellants. IV. Effect of the nature of nitramines on aluminum agglomeration and combustion efficiency. *Combust. Eeplo. Shock.* **42**(4), 436–449 (2006).
18 Glotov, O. G. Condensed combustion products of aluminized propellants. II. Evolution of particles with distance from the burning surface. *Combust. Eeplo. Shock.* **36**(4), 476–487 (2000).
19. Glotov, O. G. Condensed combustion products of aluminized propellants. III. Effect of an inert gaseous combustion environment. *Combust. Eeplo. Shock.* **38**(1), 92–100 (2002).
20. Babuk, V. A., Dolotkazin, I. N. & Glebov, A. A. Burning mechanism of aluminized solid rocket propellants based on energetic binders. *Propell. Explos. Pyrot.* **30**(4), 281–290 (2005).
21. Liu, M. Y., Yu, W. H. & Li, S. P. Effect of aluminum-based additives on the ignition performance of ammonium perchlorate-based composite solid propellants. *Acta Astronaut.* **204**(159), 321–330 (2023).
22. Baker, K. L., Hermsen, R. W. & Willoughby, P. G. Photographic study of solid propellants burning in an acceleration environment. *Sym. Combust.* **13**(1), 1033–1045 (1971).
23. Salita, M. Survey of recent Al_2O_3 droplet size data in solid rocket chambers, nozzles, and plumes. In *21st Jannaf Exhaust Plume Technology Meeting* (1994).
24. Beckstead, M. W. A model for solid propellant combustion. *Sym. Combust.* **18**(1), 175–185 (1981).
25. Cohen, N. S., & Strand, L. D. A model for the burning rates of composite propellants. In *17th Jannaf Combustion Meeting.* **1**, 53–97 (1980).
26. Crump, J. E., Prentice, J. L. & Kraeutle, K. J. Role of scanning electron microscope in study of solid propellant combustion: Behavior of metal additives. *Combust. Sci. Technol.* **1**(3), 205–223 (1969).
27. Grigorev, V. G., Kutsenogii, K. P. & Zarko, V. E. Model of aluminum agglomeration during the combustion of a composite propellant. *Combust. Eeplo. Shock.* **17**(4), 356–363 (1981).
28. Duterque, J. Experimental studies of aluminum agglomeration in solid rocket motors. *Int. J. Eenrg. Mater. Ch.* **4**(1–6), 693–705 (1997).
29. Babuk, V. A., Dolotkazin, I. N. & Sviridov, V. V. Simulation of agglomerate dispersion in combustion of aluminized solid propellants. *Combust. Eeplo Shock.* **39**(2), 195–203 (2003).
30. Babuk, V. A., Dolotkazin, I. N. & Nizyaev, A. A. Analysis and synthesis of solutions for the agglomeration process modeling. *Prog. Propuls. Phys.* **4**(1), 33–58 (2013).
31 Jackson, T. L., Najjar, F. & Buckmaster, J. New aluminum agglomeration models and their use in solid-propellant-rocket simulations. *J. Propul. Power.* **21**(5), 925–936 (2005).
32. Xiao, L. Q. *et al.* Cluster analysis of Al agglomeration in solid propellant combustion. *Combust. Flame.* **203**(2), 386–396 (2019).
33. Gallier, S. A stochastic pocket model for aluminum agglomeration in solid propellants. *Propell. Explos. Pyrot.* **34**(2), 97–105 (2009).
34. Gallier, S. & Yiao, M. Aluminum agglomeration model calibration with improved experimental data. *J. Propul. Power.* **29**(5), 1252–1255 (2013).
35. Liu, M. Y., Yu, W. H. & Li, S. P. Factors in condensate product particle size during aluminized propellant combustion. *AIAA J.* **61**(8), 1–11 (2023).
36. Levitas, V. I., Pantoya, M. L. & Dikici, B. Melt dispersion versus diffusive oxidation mechanism for aluminum nanoparticles: Critical experiments and controlling parameters. *Appl. Phys. Lett.* **92**(1), 064903 (2008).
37. Wang, J. L., Wang, N. F., Zou, X. R., Yu, W. H. & Shi, B. L. Modeling of micro aluminum particle combustion in multiple oxidizers. *Acta. Astronaut.* **189**, 119–128 (2021).
38. Wang, J. L. *et al.* Experimental and numerical study on slag deposition in solid rocket motor. *Aerosp. Sci. Technol.* **122**(5), 107404 (2022).
39. Zhang, S. & Dreizin, E. L. Reaction interface for heterogeneous oxidation of aluminum powders. *J. Phys. Chem. C.* **117**(27), 14025–14031 (2013).
40 Tu, C. Y. *et al.* Thermal decomposition, ignition process and combustion behavior of nitrate ester plasticized polyether propellant at 0.1–3.0MPa. *Int. J. Aerospace Eng.* **2022**, 6439787 (2022).
41. Li, L. B., Chen, X., Zhou, C. S., Li, W. X. & Zhu, M. Experimental and model investigation on agglomeration of aluminized fuel-rich propellant in solid fuel ramjet. *Combust Flame.* **219**, 437–448 (2022).

Acknowledgements

Tu Chengyin wishes to express the thanks to the China Postdoctoral Science Foundation (Certificate Number: 2023M731674) and the Jiangsu Funding Program for Excellent Postdoctoral Talent.

Author contributions

C.-y.T.:Methodology, Data curation and Writing-Original draf preparation; X.C.:Conceptualization and Supervision; F.C.:Date curation; Y.-q.Z.:Data curation; W.-x.C.:Supervision; Y.-k.L.:Validation; W.-x.L.:Editing and validation; C.-x.Z.:Supervision; R.-j.X:Editing. All authors reviewed the manuscript.

Competing interests

The authors declare no competing interests.

Additional information

Correspondence and requests for materials should be addressed to X.C.

Reprints and permissions information is available at www.nature.com/reprints.

Publisher's note Springer Nature remains neutral with regard to jurisdictional claims in published maps and institutional affiliations.

Open Access This article is licensed under a Creative Commons Attribution-NonCommercial-NoDerivatives 4.0 International License, which permits any non-commercial use, sharing, distribution and reproduction in any medium or format, as long as you give appropriate credit to the original author(s) and the source, provide a link to the Creative Commons licence, and indicate if you modified the licensed material. You do not have permission under this licence to share adapted material derived from this article or parts of it. The images or other third party material in this article are included in the article's Creative Commons licence, unless indicated otherwise in a credit line to the material. If material is not included in the article's Creative Commons licence and your intended use is not permitted by statutory regulation or exceeds the permitted use, you will need to obtain permission directly from the copyright holder. To view a copy of this licence, visit http://creativecommons.org/licenses/by-nc-nd/4.0/.

© The Author(s) 2024